Received: 11 August 2025 | Revised: 18 December 2025 | Accepted: 22 December 2025

DOI: 10.1002/rpm2.70039

RESEARCH ARTICLE

RESPONSIVE MATERIALS Open Access WILEY

4D printing of fast-responsive liquid crystalline elastomers for light-driven actuators

Giovanni Simonetti[1,2] | Ruggero Rossi[1,3] | Daniele Martella[1,3] | Caterina Credi[1,4] | Cecilia Ferrantini[5] | Federico Carpi[6] | Camilla Parmeggiani[1,3]

[1]European Laboratory for Non Linear Spectroscopy (LENS), Sesto Fiorentino, Italy

[2]Department of Physiscs and Astronomy, University of Florence, Sesto Fiorentino, Italy

[3]Department of Chemistry "Ugo Schiff", University of Florence, Sesto Fiorentino, Italy

[4]National Institute of Optics, National Research Council (INO-CNR), Sesto Fiorentino, Italy

[5]Department of Experimental and Clinical Medicine, University of Florence, Florence, Italy

[6]Department of Industrial Engineering, University of Florence, Florence, Italy

Correspondence

Ruggero Rossi and Camilla Parmeggiani.
Email: ruggero.rossi@unifi.it and camilla.parmeggiani@unifi.it

Abstract

Among smart materials, Liquid Crystalline Elastomers (LCEs) combine programmable well-defined deformations with wireless control. To date, the successful fabrication of LCEs through 3D printing techniques, such as direct ink writing (DIW), requires precise control over the ink formulation, mesogen alignment, and curing processes, to get devices with uniform molecular orientations, and with optimized actuation performance. Here, we present a simple synthetic approach leading to a ten-of-gram-scale ink production suitable for low-cost DIW 3D printing of LCEs. The novel ink, containing a push-pull azobenzene directly linked to the polymer backbone, enabled 4D printing of fast responsive photomechanical actuators with programmable and reversible deformation. Our centimeter-scale LCE structures present active tensions twitches comparable to those of cardiac muscles, both in terms of magnitude (kPa range) and timescale (tens to hundreds of milliseconds). An all-round actuation characterization is also developed and reported. As a proof-of-concept demonstrator, an optical beam steerer was developed demonstrating a high control of the beam diffraction angle as a function of the control beam light power.

Keywords

4D printing, light-actuation, liquid crystalline elastomers, photoresponsive materials, smart polymers

1 | INTRODUCTION

3D printing of responsive materials (the so-called 4D printing when the printed structures react by external stimuli and change its form accordingly) has emerged as an innovative approach for fabricating smart structures capable of dynamic and programmable shape changes in response to external stimuli, such as heat, light, or electric fields. This additive manufacturing technology enables precise control over material composition and device architecture, allowing for the creation of complex geometries and spatially tailored properties. Among the most versatile responsive materials, Liquid Crystalline Elastomers (LCEs) are a class of cross-linked polymers presenting the anisotropic properties of liquid crystals (e.g., birefringence) and the mechanical behavior of elastomers.[1–3] This combination allows LCEs to undergo controlled and reversible shape changes in response to various external stimuli, as shown in Figure 1. As *smart materials*, LCEs are extensively proposed for soft robotics,[4] wearable sensors,[5] artificial muscles,[6] biomimetics[7] and optical devices.[8]

Thanks to the predetermined alignment of mesogenic units within the elastomeric matrix, deformations or mechanical responses to the external stimulation can be highly

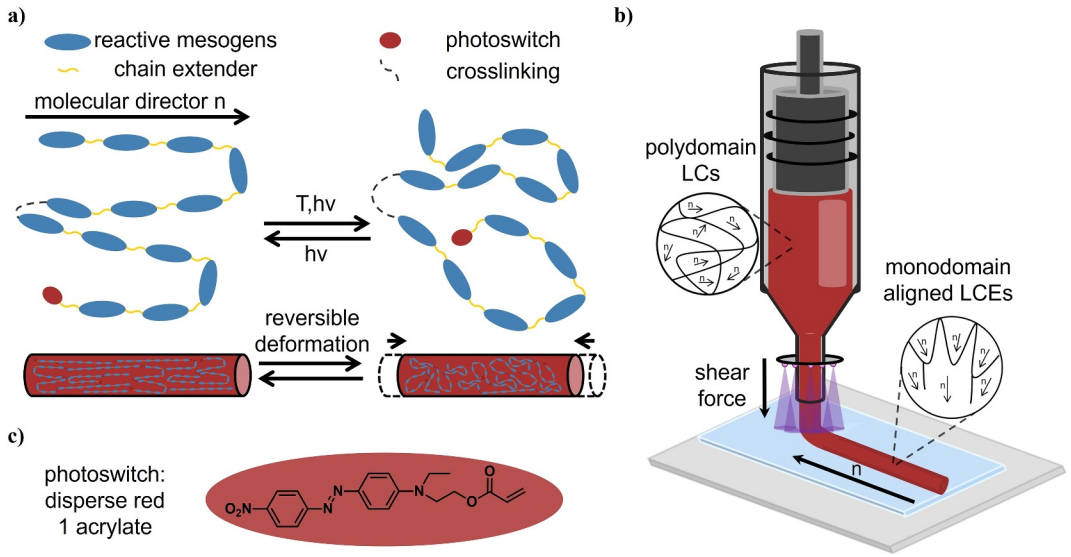

FIGURE 1 A general overview of the 3D printing of LCEs. (a) Illustration of the LCE structure and of its activation when exposed to a stimulus; the material contracts along the nematic director that was aligned during the extrusion process. (b) Representation of the 3D printing process: during extrusion, shear forces caused by the ink flow allow the polymer main-chain to align along the printing path; (c) Molecular structure of the disperse red 1 acrylate photoswitch used in this work. LCE, liquid crystalline elastomer.

controllable and arbitrary designed, for example, showing contraction along the liquid crystalline (LC) directors in homogeneous planar aligned samples (Figure 1a).

In general, LC order inside these polymers can be presented in a polydomain or a monodomain fashion, as shown in Figure 1b. In the polydomain state, mesogens are arranged in randomly oriented domains, each with its own alignment direction. This randomness results in overall isotropic properties, limiting the (anisotropic) actuation capabilities of the material. On the other hand, monodomain LCEs are defined by mesogen alignment along a single direction throughout the material, called director (*n*). Transitioning from a polydomain to a monodomain state is a key step for programmable actuation. This can be achieved through different strategies, including surface anchoring,[9] mechanical stretching,[10] magnetic or electric fields,[11] or shear stress during fabrication,[12] which aligns the mesogens before curing (that lock molecular order). External stimuli like heat,[13] light[14] or magnetic field[15] can partially disrupt the order of the LC domains, causing controlled deformation along the alignment axis. After the stimuli removal, the original LC order is restored thanks to the crosslinked system leading to the recovery of the initial shape. This enables programmable, reversible shape changes, making monodomain LCEs ideal for applications like actuators[16] and optical devices.[17] Indeed, recent advancements in thermally responsive LCEs have demonstrated their capability to perform several robotic tasks, such as walking,[18] crawling and rolling,[19] gripping,[20] and lifting,[21] enabled by complex 3D shapes and designs.

The most common approach for fabricating LCE films involves infiltrating an LC mixture into a cell where alignment is ensured by surface anchoring. However, this method can produce only films (thinner than 100 μm), while 3D shaping is prevented.

In recent years, this disadvantage have been overcome thanks to the introduction of 3D printing, using different methods, such as Direct Ink Writing (DIW),[22,23] Digital Light Processing,[24,25] and Inkjet Printing.[26] Among them, DIW allows for high flexibility and precision, combined with cheap instrumentation, which have driven a drastic increase in the study of this technique for the fabrication of 4D printed LCEs. During the DIW process (schematically illustrated in Figure 1b), an LC-based ink is extruded through a nozzle, and the mesogens align along the printing path, due to shear stresses generated during extrusion. This method enables the creation of structures with uniform thickness and polymer chains aligned parallel to the printing direction. DIW supports the fabrication of complex geometries, gradients in material properties, and programmable actuation patterns, allowing printed structures to bend,[5,27] twist,[28,29] or expand[30,31] in response to stimuli.

Concerning the chemistry of the ink, the type of mesogens can be engineered to modulate the phase transition (and thus the temperature range of the deformation),[32] while, in some cases, introducing a vinyl crosslinker can initiate a thiol-ene reaction to further refine the cross-linking process.[23] Cross-linking is typically completed after printing via photoinitiators, ensuring structural stabilization and elastomeric functionality.

Moreover, incorporating photosensitive molecules or nanoparticles extends the responsiveness of printed LCEs to light, offering high spatial resolution for actuation without direct contact. In particular, nanoparticles such as gold can be incorporated to absorb near-infrared (NIR) light and convert it into localized heat, up to 160°C.[33] This thermal

effect can drive actuation, making it well-suited for soft robotics applications by enabling high photothermal efficiency, substantial work capacity, and stability across repeated actuation cycles.[33,34]

On the other hand, the addition of an azobenzene molecule, such as disperse red 1 acrylate (DR1A, Figure 1c), can induce actuation through two distinct mechanisms: photochemical and photothermal.[35] The photochemical effect involves *trans-cis* isomerization upon light exposure, disrupting LC order and triggering a deformation. The photothermal effect derives from light absorption by the dye, which generates localized heat and induces shape changes. While both effects contribute to actuation, the photochemical one provides precise molecular control, making it preferable in thermally-sensitive environments (e.g., in biomedical devices). Recent studies have demonstrated that azobenzene can induce shape changes in LCEs through a photochemical mechanism under moderate-intensity UV light. This allows actuation in water with minimal thermal effects, enabling advanced motion across various environments.[36]

This study describes 4D-DIW of photoresponsive LCEs capable of response times to visible light shorter, to the best of our knowledge, than those previously reported for other photoactivated LCEs.[37] This was possible by incorporating a push-pull azobenzene dye (DR1-acrylate), enabling LCE structures to respond to 470 nm blue light, while reverting to their original state upon light removal, eliminating the need for additional light sources or prolonged thermal recovery.[38] Additionally, the system can operate at temperatures between 29 and 44°C during irradiation, addressing the problem of high thermal outputs typically observed in azobenzene-based systems,[7] which can limit their suitability for biomedical applications. The light-responsive behavior of the material was studied across both second and sub-second timescales of irradiation, with the view of targeting potential applications in optical devices and muscle-mimicking systems. Although LCE-based devices with response times in the millisecond or microsecond range have already been demonstrated,[39–41] such rapid responses have not yet been reported for 4D printed LCEs prepared by DIW. As a proof-of-concept demonstration of the LCEs reversible photoactuation and their potential for optical applications, a light beam steering device driven by photoactuation is presented.

2 | RESULTS AND DISCUSSION

2.1 | LC-based ink synthesis and characterization

The printable LC ink was formulated through the reaction between two nematic diacrylate mesogens and an aliphatic dithiol (all chemical structures are shown in Figure 2a). The molecular ratio was set at 1:1.2 with the excess of the acrylate groups ensuring the final crosslinking density. More in detail, the diacrylate amount was given by 75% in moles of RM82 (a commercially available mesogen) and 25% in moles of (1,4-bis-[4-(6-acryloyloxyhexyloxy)benzoyloxy]-2-phenylbenzene) (CL6-Ph, a reactive mesogen recently introduced by some of us), respectively. The presence of CL6-Ph introduced unique properties in the ink. It lowered the T_{NI}, thus reducing the energy input required for actuation and enhancing photoactuation performance in terms of speed and generated tension (see Section 2.4 below). It also stabilized the LC phase at room temperature, therefore preventing crystallization and enabling easier processing. Compared to a similar formulation without the phenyl monomer (previously studied in our laboratory),[42] the new material showed a markedly improvement of the overall performance, presenting more pronunced thermal contraction (35% of the initial length, vs. 10% for the reference material under identical conditions) and enhanced maximum stress generated during photoactuation (increased by a factor of 25, rising from 14 to 350 kPa).[32]

The mixture was completed with the UV photoinitiator (Irgacure 819, 2 wt%), the azobenzene dye (disperse red 1 acrylate, DR1A, 1 wt%) and dissolved in dichloromethane (DCM). Then, the thiol chain extender ethyleneglycolbis-mercaptoacetate (EGM) and the base catalyst (1wt% triethylamine, TEA) were added to the solution and stirred at 50°C for 2 h (Figure 2b). The oligomeric solution was subjected to a liquid-liquid separation with an acid solution to extract the TEA. More details about the reaction procedure and oligomer purification are reported in the Supporting Information S1, together with its ^{1}H-NMR spectrum (Figure S1).

Properties of the LC ink were investigated using Polarized Optical Microscopy (POM) and Differential Scanning Calorimetry (DSC). By integrating the results from both methods, the LC phase types with relative transition temperatures were identified, as evident from Figure 2c,d. Schlieren textures typical of the nematic phase were observed via POM around 50°C, and the isotropic phase was seen at 70°C. By DSC measures, a single endothermic peak at 60°C (both on heating and cooling) was noted, indicating the nematic-to-isotropic phase transition (T_{NI}). The determination of T_{NI} is fundamental for the printing process, as an optimal mesogen alignment is achieved when the ink is printed in its nematic phase. Therefore, all structures were printed at temperatures below 60°C to ensure proper alignment.

2.2 | 3D DIW and LCE characterization

A systematic investigation on the printing speed was performed as it directly influences shear forces on the ink, playing a crucial role in achieving a monodomain molecular alignment. The LCE structures were fabricated using the Hyrel 3D Engine Standard Resolution (ESR) printing system (Figure 3a), equipped with a 25G nozzle (inner diameter 0.254 mm), a screwball-driven mechanism operating at 1400 rpm, and an extrusion temperature of 60°C. During

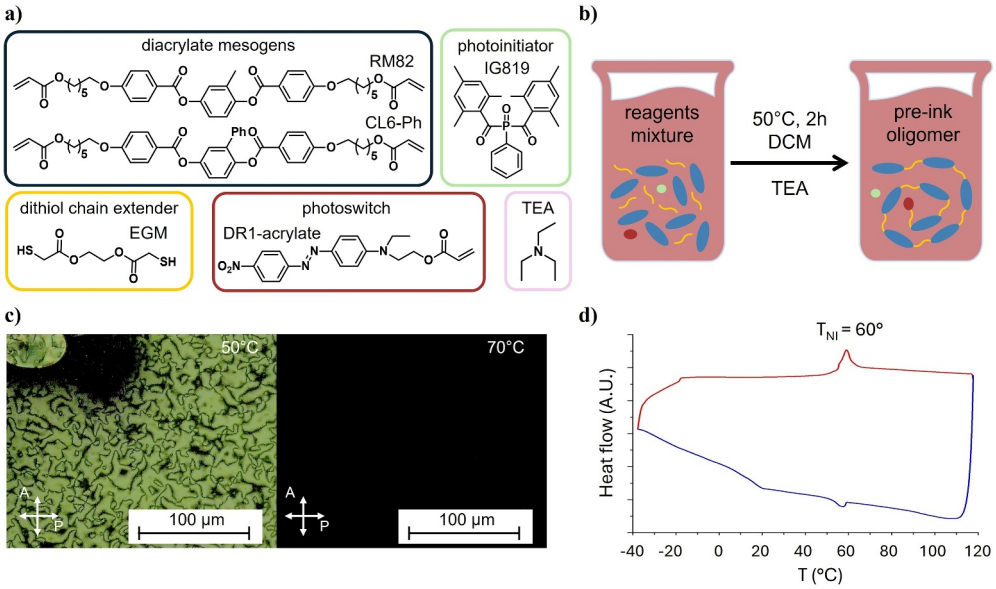

FIGURE 2 Synthesis and characterization of the LC ink. (a) Molecular structures of the ink components; (b) Representation of the reaction condition; (c) polarized optical microscopy images of the LC ink in the nematic phase (left) at 50°C and in the isotropic phase (right) at 70°C; (d) differential scanning calorimetry trace of the oligomer, first cycle on heating and cooling, exo down. LC, liquid crystalline.

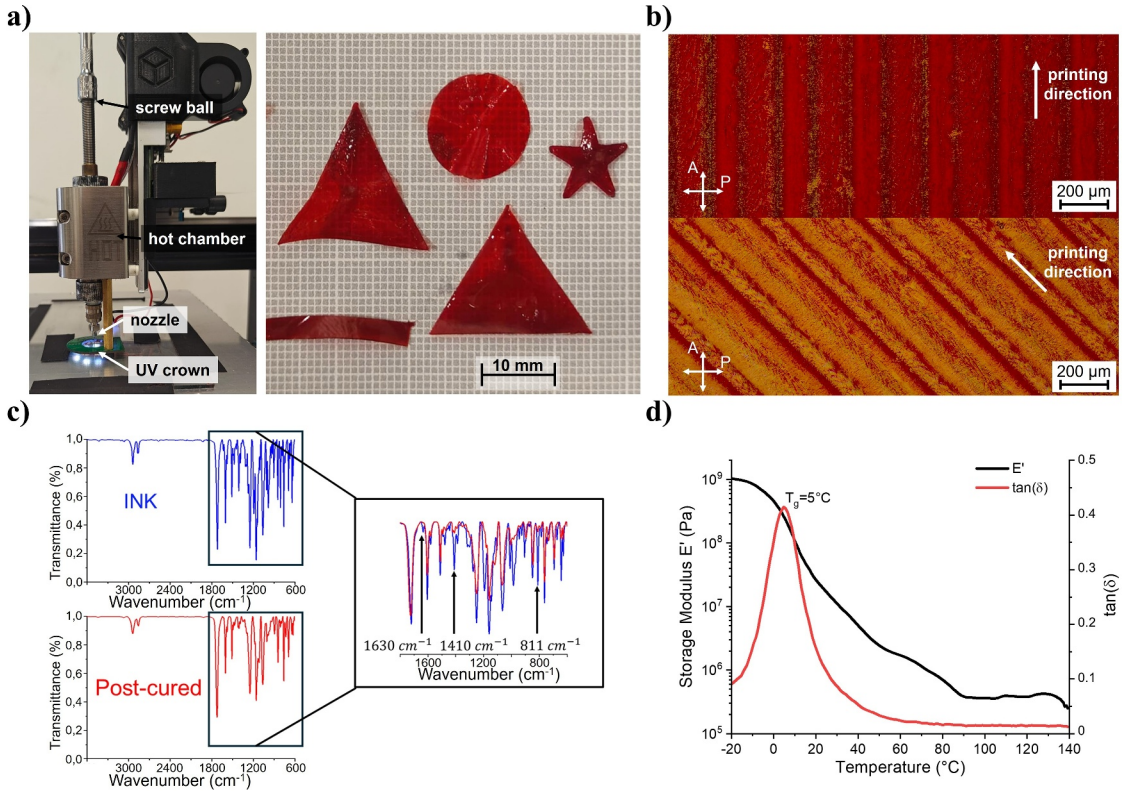

FIGURE 3 Direct ink writing of LCEs and characterization of the printed structures. (a) Image of the printing head of the Hyrel 3D engine standard resolution printer and LCE printed structures; (b) polarized optical microscopy images of a printed LCE at 0° (up) and 45° (down) with respect to one polarizer axis. The alignment is confirmed by the change of transmittance in between the two orientations; (c) FTIR spectra of the liquid crystalline ink and of the post-cured LCE, highlighting the weakening of the peaks corresponding to acrylate group signals (1630 cm^{-1}, 1410 cm^{-1} and 811 cm^{-1}), demonstrating the crosslinking given by the post-curing process; (d) dynamic mechanical analysis analysis carried out in tension mode at a temperature rate of 5°C/min. The graph shows the storage modulus curve E′ and tan(δ) as functions of the temperature. The tan(δ) peak corresponds to T_g. LCE, liquid crystalline elastomer.

extrusion, an UV crown was used to irradiate the sample and induce an initial curing of the material. The resulting partial curing stabilized the printed structure, preventing nozzle clogging. As shown in the Supporting Information S1: Figure S2A, POM images of strips printed at various speeds clearly demonstrate that a printing speed of 2 mm/s resulted in a lack of molecular alignment, while speeds equal or higher than 8 mm/s led to an inadequate material deposition. Therefore, an optimal balance to ensure the material deposition accuracy (defined as the combination of the XY accuracy and of the filament accuracy, as reported in the Supporting Information S1: Figures S2A and S2B) and a proper LC alignment was offered by a printing speed between 4 and 6 mm/s. The printed samples were observed under POM, in cross-polarized configuration, in order to evaluate the molecular alignment through the variation of transmittance, as shown in Figure 3b. The presented photos were taken on a 50-micron-thick sample, which clearly showed the printing lines. The variation in transmittance between LC orientations along 0° and 45° relative to a polarizer axis confirmed the mesogens alignment. In the best printing conditions (6 mm/s printing speed, 25G nozzle, 1400 rpm, and 60°C), the average order parameter (S), determined by UV–vis polarized spectroscopy (Supporting Information S1: Figure S3A), was $S = 0.77 \pm 0.05$.

A post-curing step with UV light (Thorlabs M385LP1) for 20 min was performed to complete the acrylate conversion. The UV LED had an emission peak at 385 nm, whereas the azobenzene dye showed a maximum absorption at 490 nm. As shown in Supporting Information S1: Figure S3B, the LED emission fitted with a minimum in the dye absorption spectrum. Although we were unable to directly monitor the isomerization process, the occurrence of a good alignment (not affected by dye isomerization) was demonstrated by POM (Figure 3b) and UV–vis spectroscopy (see order parameter determination in Supporting Information S1: Figure S3A), while the crosslinking completion was confirmed by ATR (Figure 3c). In particular, the occurrence of cross-linking was assessed using Fourier Transform InfraRed (FTIR) spectroscopy by comparing the characteristic peaks of the acrylate group in the spectra of the LC ink and the printed LCE. Figure 3c shows a reduction in the peaks at 1630 cm^{-1}, 1410 cm^{-1} and 811 cm^{-1} (typical of the acrylate groups) in the printed sample (red) if compared with the mixture (blue).

DSC measurements of the cured polymer, as shown in Supporting Information S1: Figure S4, were conducted across a temperature range from −20°C to 200°C. They showed the absence of any detectable peaks and confirmed the complete curing and the absence of degradation or phase transitions within that temperature range, as expected for crosslinked polymers.[43]

The thermomechanical properties of the LCE were studied using dynamic mechanical analysis (DMA), where the storage modulus (E′) and tan(δ) were measured as a function of temperature, as shown in Figure 3d. This analysis showed that the LCE exhibited a glass transition temperature below room temperature (T_g = 5°C) and a storage modulus in the MPa range (E' = 17 MPa at 25°C), thereby retaining the mechanical characteristics typical of viscoelastic materials.

2.3 | Thermo-actuation

LCEs typically exhibit structural shape changes when they are heated beyond a specific temperature. This occurs due to a reduction in the orientational order of the mesogens, resulting in a contraction along the molecular director (n) and in an expansion in the direction perpendicular to it. To evaluate the LCE deformation under thermal stimuli, rectangular samples (10 × 3 × 0.05 mm) were heated on a hot plate and photographed every 10°C, as illustrated in Figure 4a. The graph displays the temperature dependence of the LCE sample normalized length (i.e., the ratio between the sample length L at a given temperature and its length at room temperature L_0). Increasing temperatures led to a gradual increase in contraction, which reached a plateau region at approximately 150°C, where the sample experienced its maximum strain (around 35%). This plateau corresponded to the limit of mesogenic order disruption in the nematic phase, such that further temperature increases were unable to cause additional deformation.

After cooling the samples back to the room temperature, a complete shape recovery was observed, demonstrating the process reversibility.

DIW was used to create complex alignment patterns, such as triangular or star-shaped geometries with perimeter infill, as shown in Figure 4b, exhibiting out-of-plane deformation (2D-to-3D actuation). On the other hand, a triangle obtained by rectilinear infill (Supporting Information S1: Figure S5) presented a 2D actuation, demonstrating different extrusion patterns to allow for different mesogen alignments and, therefore, different (and programmable) movement. All the presented structures responded rapidly, reversibly, and in a programmable way to external stimuli such as light or temperature (Movie S1 and Supporting Information S1: Figure S5), allowing for the design of more complex LCE-based devices with multi-responsive capabilities.

2.4 | Photo-actuation

Our main interest in using light-responsive 4D-printed LCEs was for an optical driving and for mimicking natural muscles from an actuation standpoint, in terms of generated stress, strain and response time, both in the second and sub-second time scales. For example, it would be of interest to mimic the heart muscle contraction, which in a regular cycle of 250 milliseconds develops, by cardiac lamellar tissues, tensions of about 1–15 kPa.[44,45]

A photomechanical characterization of the LCEs was done by a custom setup previously designed to measure tension

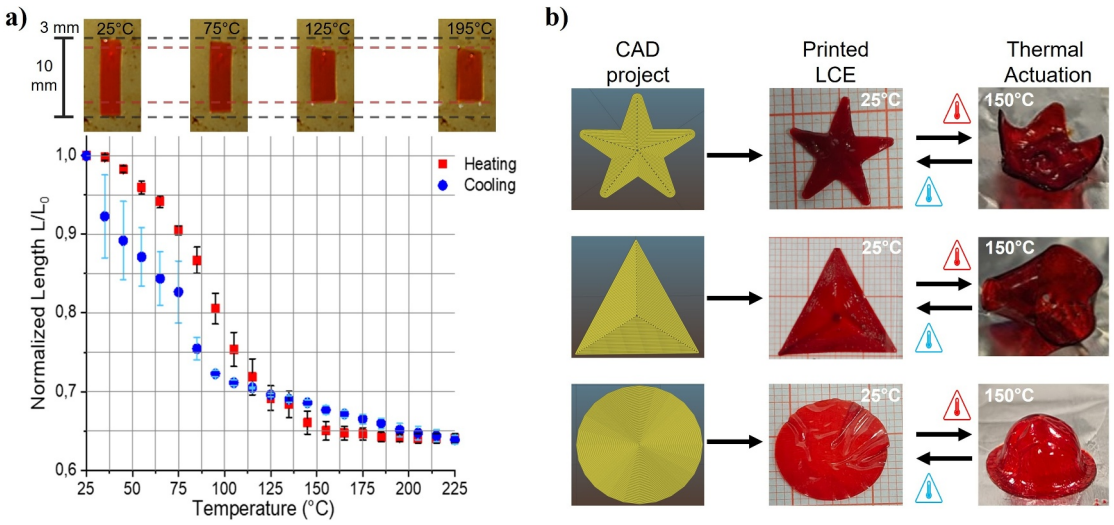

FIGURE 4 LCE thermal actuation. (a) Thermal contraction and relaxation of an LCE rectangular sample heated and cooled at a rate of 10°C/min; (b) Thermally induced out-of-plane actuation at 150°C of LCE printed samples with perimetral infill pattern. LCE, liquid crystalline elastomer.

under isometric conditions.[46,47] LCE strips (20 × 1.2 mm) were vertically mounted between a force transducer at the top and a fixed end at the bottom, as shown in Figure 5a. The sample was positioned between two LEDs emitting light at 470 nm at different optical power densities. A first test was performed on 50 µm-thick strips to evaluate the relationship between tension and the LED optical power density. The first set of measurements was conducted in sequence of cycles, where each cycle consisted of 8-s illumination, followed by 2 s without light, as shown in Figure 5b. The tension raised progressively during illumination, and it reached a plateau after approximately 5 s. Upon switching the light off, the tension rapidly returned to zero within approximately 2 s. As expected, the developed tension increased with the applied intensity of the light; in particular, it was observed that the maximum stress generated at the highest light intensity (6.2 mW/mm^2) was approximately three times greater than that at the lowest intensity (2.3 mW/mm^2), as shown in Figure 5b. To demonstrate the repeatability of actuation, the LCE strip was irradiated for 8s within 2-s intervals over 20 consecutive cycles. The graph in Supporting Information S1: Figure S6 illustrates the results from the first 4 cycles, showing that the recorded twitches of tension followed a consistent pattern, with the maximum developed stress reaching approximately 350 kPa.

The same experiment was repeated for the LCE strips with a thickness of 100 and 150 µm, to evaluate how the sample thickness influenced the generated tension, the steady-state response time (SSRT), as well as the short-pulse actuation speed (SPAS). The SSRT was defined as the time needed to reach 90% of the tension at the plateau, while the SPAS was defined (in analogy with natural muscle behavior) as the initial slope (first 200 ms of irradiation) of the tension curve,[32] where the tension showed an initial linear trend. These properties were analyzed depending on the sample thickness and the intensity of the applied light. The results are summarized in Supporting Information S1: Table S1.

Figure 5c shows that the SSRT was significantly more influenced by the strip thickness than by the applied optical power density. Samples with a thickness of 50 µm exhibited SSRTs of approximately 3.5 s, independently of the optical power density. In contrast, 100 µm-thick samples displayed longer SSRTs (between 4 and 4.5 s), increasing with the light source intensity. For 150 µm-thick samples, an increase of optical power density caused an increase in SSRT from 4.8 to 5.3 s. According to the literature on photoresponsive LCEs, these values represent relatively fast responses to light stimulation.[38]

The results of the SPAS characterization are reported in Supporting Information S1: Tables S1 and S2, as well as Figure 5d. They show that the sample thickness and the applied optical power density significantly affected the SPAS and the maximum tension developed by the materials. Thinner samples (50 µm) exhibited higher tension and greater SPASs at lower power densities, reaching ~334 and 229.1 kPa/s at 6.2 mW/mm^2. In comparison, 100 µm-thick samples under the same conditions generated 185 kPa tension and a SPAS of 94.1 kPa/s, while 150 µm-thick samples achieved <100 and 16.6 kPa/s.

The samples with a thickness of 50 µm were the most fragile, breaking after a few irradiation cycles at an optical power density of 7.8 mW/mm^2. In contrast, thicker samples tolerated higher intensities, up to 15.9 mW/mm^2. This increased resistance to light intensity was accompanied by slower SPASs, likely due to reduced light penetration. At the maximum power, 100 and 150 µm-thick samples reached peak tensions of 437 and 306 kPa, with SPASs of 148.5 and 89.7 kPa/s, respectively. Thinner samples presented higher tensions and SPAS at lower light intensities, although they were more susceptible to failure at high power levels. Thicker samples, although capable of withstanding higher power inputs, developed lower tensions and were slower, due to limited light penetration. Therefore, the SPAS analysis provided insights into the material response dynamics,

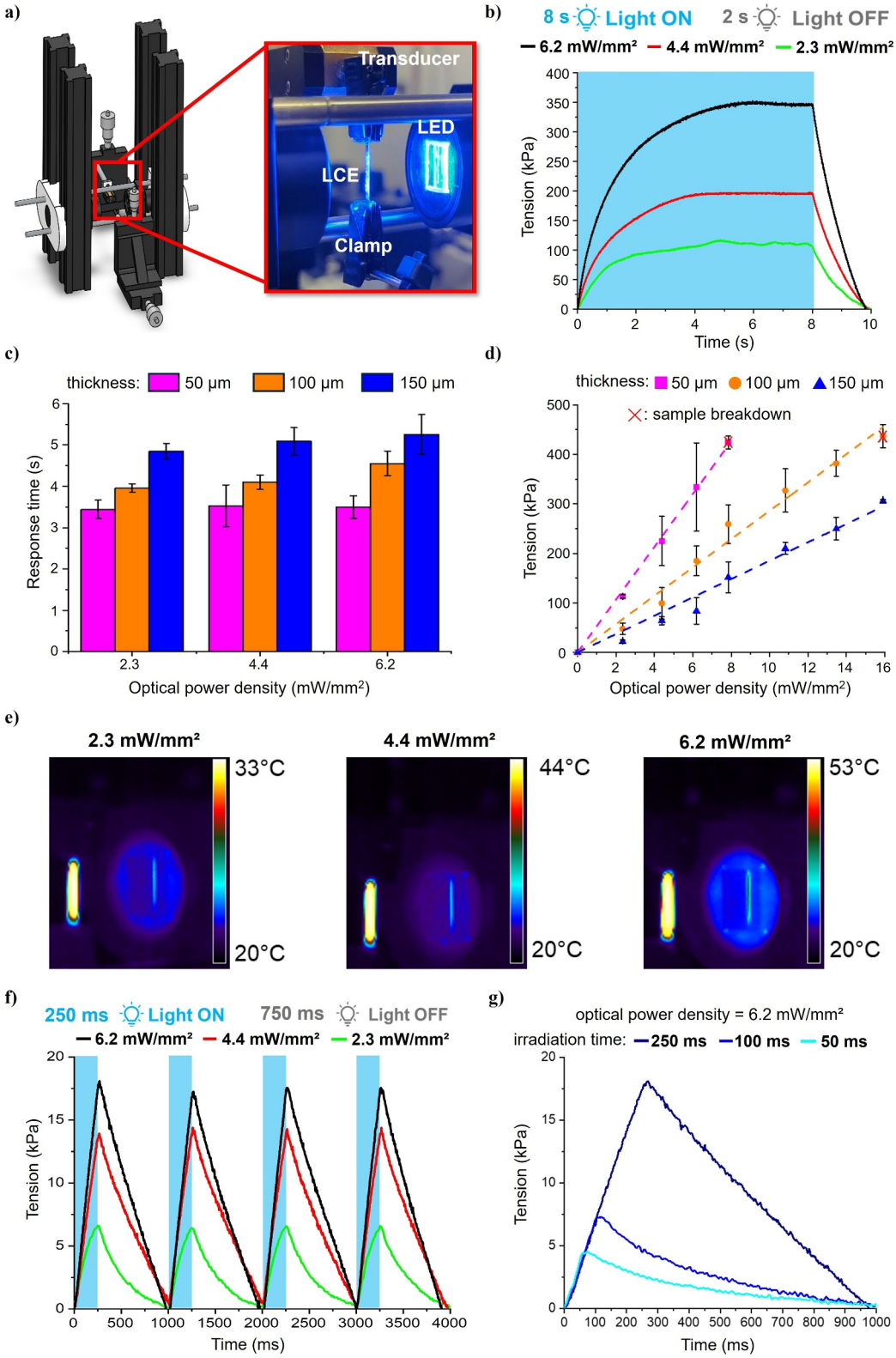

FIGURE 5 Photoactuation of LCE strips. (a) Drawing and photo of the test set-up; (b) LCE sample (12 × 2 × 0.05 mm) under 8 s activation with different optical powers; (c) LCE steady state response time as a function of the applied optical power density and the sample thickness; (d) Developed tension versus sample thickness and optical power density; (e) Thermal images of a 100 µm-thick sample under three different optical power densities during 8-s irradiation time; (f) Short and cyclical activation of 50 µm-thick LCE with 250 ms pulses at varying optical power densities; (g) Activation of 50 µm-thick LCE using short pulses (50, 100 and 250 ms) at fixed optical power densities. LCE, liquid crystalline elastomer.

highlighting a trade-off between rapid response and tension development in LCEs, and showing how 100 μm-thick samples were the best choice towards applications requiring both robustness and responsiveness.

In general the mechanism behind LCE force production can involve both a photochemical effect (due to the disordering induced during the *cis-trans* isomerization) and a photothermal one (dissipation of light into heat), to gain an insight into the dominating mechanism in our experimental conditions, the LCE strip temperature was monitored during isometric photoactuation. Figure 5e presents thermal images corresponding to an LCE with a 100 μm thickness driven at the three different optical power densities (2.3, 4.4, and 6.2 mW/mm^2) during an 8-s irradiation period. Interestingly, upon irradiation, the sample exhibited temperature increases of 13°C and 24°C when illuminated at light intensities of 2.3 mW/mm^2 and 4.4 mW/mm^2, respectively; indeed, the sample temperature increased from room temperature (20°C) to 33°C and 44°C, respectively. At the highest tested intensity (6.2 mW/mm^2), the temperature rose by 33°C, reaching 53°C. In Supporting Information S1: Figure S7 are reported the results of the same experiment repeated with 50 and 150 μm thick samples. As expected, the temperature increase upon irradiation strongly depends on the optical power density and only slightly on the sample thickness. No significant differences were observed between the 50 μm and 100 μm-thick samples. However, the 150 μm-thick samples showed lower temperature increases (9°C, 18°C, and 28°C) as the optical power density increased. This reduction was likely due to reduced light penetration in thicker films, which also promoted a more efficient heat dissipation. During photoactuation, the material exhibited its highest tensile response at 55°C (corresponding to an optical power density of 6.2 mW/mm^2, Figure 5b,e), suggesting that the actuation relies mainly on a light-driven molecular mechanisms (isomerization) and is supported by a moderate thermal effect. These findings were also supported by the thermal analysis of the star (obtained by perimetral infill, optical actuation also reported in Movie S1) activated by a single LED (450 nm, light intensity 4.7 mW/mm^2) irradiation. As reported in Supporting Information S1: Figure S8 the temperature under these conditions did not exceed 37°C, far below the level required for significant thermally driven deformation (150°C, as reported in Figure 4a).[35, 48]

A second characterization test was performed under short-pulse actuation, a condition that is relevant for artificial muscle development. Based on previous results, the 50 μm thick samples (showing the highest SPAS at low optical power densities) were selected for this study. As shown in Figure 5f, an irradiation cycle of 250 ms followed by 750 ms of rest produced consistent and repeatable actuation over 4 cycles (20 cycles are shown in Supporting Information S1: Figure S9A), with linear tension development and relaxation. Increasing the optical power density led to a progressive rise in generated tension, from 7 to 14 and 17 kPa. Remarkably, the resulting actuation profile closely resembled that of cardiac muscle twitches.[47] Furthermore, as shown in Figure 5g, the material was tested under light pulses of 50 and 100 milliseconds (followed by 950, 900 ms of relaxation, respectively) and compared to the 750 ms activation pulse cycles (optical power density of 6.2 mW/mm^2). In these conditions, the 50 μm-thick samples generated with an approximately linear profile tensions between 5 and 7 kPa, comparable to those produced by heart muscle cells (cardiomyocytes). Even in this case, repeatability was studied, as shown by the multiple activation/relaxation cycles reported in Supporting Information S1: Figures S9B,C, demonstrating the material's ability to respond effectively within tens of milliseconds, and underlining its suitability for fast and dynamic actuation scenarios.

2.5 | Beam steering by 4D printed LCEs

The applicability of our approach to optical devices was evaluated at a preliminary level by a DIW-printed LCE light beam steerer. The device was conceived to harness the actuation properties of the LCEs, to control the direction of a laser beam with a good robustness and reproducibility. A scheme of the experimental setup is shown in Figure 6a. A lightweight polystyrene piece was attached to one end of a gold-coated (by sputtering) LCE strip (13 × 2 × 0.1 mm). The obtained LCE mirror (Figure 6b) was mounted on a support with its reflective tip left free to move. In its initial state, the beam steerer reflects a red light (633 nm laser) used as a probe, at a certain angle. When triggered by a focused blue light (450 nm laser, control beam) applied from one side, the system was activated, as the strip actuated in bending mode, causing a horizontal displacement of the probe light. Depending on the power of the blue light, the displacement of the probe light changed, indicating a modulation of the reflection angle. The deflection was monitored on a panel and recorded using a camera, as shown in Figure 6c. By measuring the displacement of the reflected spot on the panel and knowing its distance from the LCE mirror, the variation in reflection angle was calculated.

The graph in Figure 6d shows the average change in the probe light reflection angle as the system changed from its initial state to its active state. This variation was plotted against the blue-laser power for three different samples. As the laser power was increased from 7.4 to a maximum value of 33.0 mW, the displacement of the reflected red laser showed a linear trend, indicating a direct proportionality between the control laser power and the displacement of the steered laser. The maximum variation in the reflection angle was measured to be 12° under a power input of 33.0 mW.

The consistency of the beam steering device was also evaluated over multiple actuation cycles. Figure 6e and Movie S2 show the angular variation of the red beam over three cycles of LCE actuation and relaxation. The results indicate a high repeatability, with the LCE consistently returning to its original position after each cycle and achieving the same angular variation during the peak actuation. The blue light-induced movements occurred in less

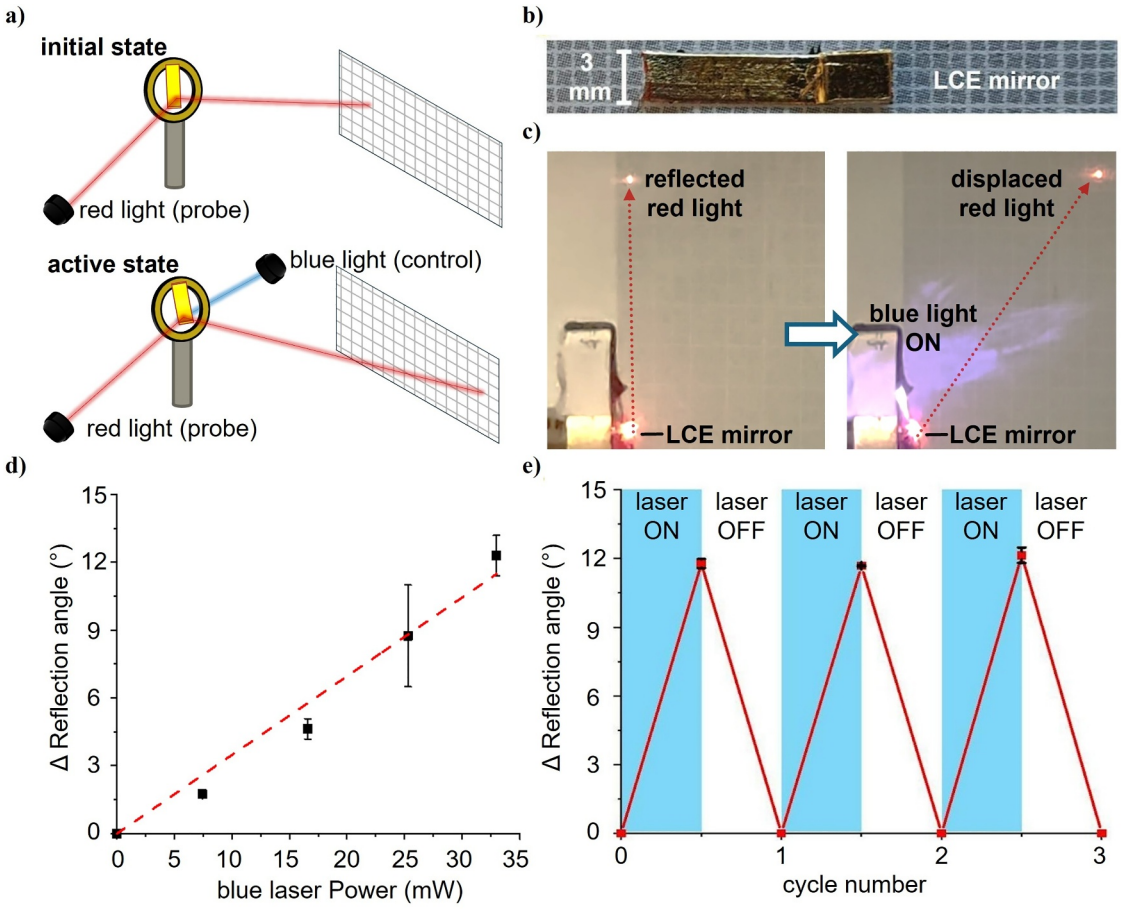

FIGURE 6 Example of programmable beam steering using an LCE-actuated bending mirror. (a) Scheme of beam steering set up; (b) Frontal photo of the beam steering set up; (c) Photo of the LCE mirror used (upper photo) and side photo of the beam steering set up, before and after the activation of the blue laser; (d) Average red light reflection angular variation as a function of the blue laser intensity; (e) Δ Reflection angle of red source during multiple cycles of LCE mirror actuation. LCE, liquid crystalline elastomer.

than a second, with the device returning to its resting position equally quickly when the laser was turned off.

3 | CONCLUSIONS

A new ink formulation was developed to obtain a DIW 4D printable LCE material capable of significant, reversible shape changes in response to thermal and optical stimuli. The thermal responsiveness of strips of the LCE material showed a maximum contraction strain of approximately −35% at 150° C. In terms of photoactuation, the LCEs generated significant tension (up to 334 kPa) under blue light in less than 10 s of irradiation in a physiologically relevant temperature range. Moreover, tensions between 5 and 17 kPa in 10 to hundred millisecond irradiation times were obtained, suggesting the applicability of our materials combined with the 3D printing technique for optical and biomedical applications.

As a proof-of-concept demonstration of a possible optical application, a LCE-driven light beam steering device was developed, illustrating the opportunity to integrate LCEs into systems for remote and contactless actuation control.

The additive nature of the DIW technique offers the potential to produce large-scale 3D structures with well-defined LC orientation, allowing for the creation of novel multiresponsive devices, with complex geometries that can be challenging to achieve with other existing LCE fabrication processes.

Future research could focus on further increasing the response speed, and investigating possible applications of devices with special 3D geometries, particularly in contexts where light or thermal stimuli can offer advantages over conventional actuation systems.

4 | EXPERIMENTAL SECTION

4.1 | Materials

1,4-bis-[4-(6-acryloyloxyhexyloxy)benzoyloxy]-2-methylbenzene (**RM82**) was purchased from Whilshire Technologies together with the chain extender ethyleneglycolbismercaptoacetate (**EGM**). 1,4-bis-[4-(6-acryloyloxyhexyloxy)benzoyloxy]-2-phenylbenzene (**CL6-Ph**) and the

azobenzene dye DR1A were obtained from Specific Polymers. The UV photoinitiator phenyl bis(2,4,6-trimethyl benzoyl), also referred to as Irgacure 819 was purchased from Sigma Aldrich, as well as the base catalyst Triethylamine (**TEA**) and dichloromethane (**DCM**). All reagents were used as received. The NMR spectra were recorded with a Varian Inova 400 MHz.

4.2 | Oligomer synthesis

1,4-bis-[4-(6-acryloyloxyhexyloxy)benzoyloxy]-2-methyl-benzene (**RM82**, 1.44 g, 2.1 mmol, 0.9 eq.), (1,4-bis-[4-(6-acryloyloxyhexyloxy)benzoyloxy]-2-phenylbenzene) (**CL6-Ph**, 0.52 g, 0.71 mmol, 0.3 eq), red 1 acrylate (**DR1A**, 24.6 mg, 0.067 mmol, 1% wt.), and phenyl bis(2,4,6-trimethyl benzoyl) (IG-819, 49.2 mg, 0.12 mmol, 2%wt.) were dissolved in dichloromethane (18 mL) with ethyleneglycolbis-mercaptoacetate (**EGM**, 0.5 g, 2.4 mmol 1.0 eq.) and triethylamine (**TEA**, 24.6 mg, 0.24 mmol, 1% wt.). The mixture was stirred at 50°C for 2 h, then some more dichloromethane was added to the mixture to dilute it and several washes with brine and hydrosulfuric acid were done. The organic layers were dried over sodium sulfate and the solvent was removed under reduced pressure. Further purifications were not necessary. A red viscous resin is obtained with a quantitative yield (2.55 g).

The total amount of diacrylates used corresponds to 1.2 M equivalents relative to 1.0 M equivalent of dithiol, while the reported weight percentages (wt%) are based on the combined mass of the three main reagents used for oligomerization: **RM82**, **CL6-Ph**, and **EGM**.

4.3 | Printing equipment

Samples were fabricated using an ESR 3D printer (Hyrel 3D), featuring an XY positional accuracy of ±50 μm and a *Z*-axis accuracy of ±10 μm. The system was equipped with a TAM high-temperature extrusion head and a UV LED array. The structures were printed on a microscope cover glass (24 × 50 × 0.1 mm) and were first photopolymerized at a wavelength of 365 nm, using the UV-LED array directly connected to the printing head; once the printing procedure was complete the samples were postcured with a UV light source of 385 nm at 0.22 mW/mm^2 (M385LP1-C4 lamp, Thorlabs) at 50°C for 10 min and at 70°C for further 10 min.

4.4 | Characterization methods

Light microscopy was performed using an inverted microscope (Zeiss Axio Observer A1) with or without cross polarizers.

The thermal transitions were measured using a DSC calorimeter TA Instruments Calorimeter Q-2000 (TA Instruments) in a nitrogen atmosphere (heating and cooling rate 20°C/min).

To identify the glass transition temperature Tg of the printed polymer, a Dynamic Mechanical Analysis (DMA 8000, PerkinElmer) was used, in which a rectangular specimen measuring 20 × 3 × 0.05 mm was tested in tensile mode. The test is carried out by heating the specimen from −30°C up to 120°C with a rate of 5°C/min. The Tg was measured at the temperature corresponding to the first peak of the tan(δ) curve, while to evaluate the crystallization temperature Tc is measured through the minimum of the derivative of the storage modulus curve (E′) at the beginning of the plateau region.

Spectra of the ink and the LCE were recorded on a PerkinElmer ATR spectrum two to evaluate the difference between diacrylate signal peaks and confirming the oligomerization from Michael's addition.

The absorption of the printed films was characterized using a UV–vis Varian Cary 400 spectrometer at room temperature. Measurements were performed on a rectangular specimen (30 × 10 × 0.05 mm). First, the non-polarized absorbance spectrum was recorded. The specimen was then mounted on a rotating support to align the printing direction at either 0° (∥) or 90° (⊥) relative to the polarized light, obtained by placing a linear polarizer in the beam path. The absorbance parallel ($A_{\parallel}$) and perpendicular ($A_{\perp}$) to the printing direction was determined at the absorption maximum (490 nm). The order parameter (*S*) was then calculated according to Equation (1):

$$S = \left(A_{\parallel} - A_{\perp}\right) / \left(A_{\parallel} + 2A_{\perp}\right) \quad (1)$$

4.5 | Thermal actuation

Temperature induced contraction tests were performed on uniaxially oriented LCE printed samples (10 mm × 3 mm × 50 μm) soaked in silicone oil on a Mettler Toledo HS82 hot plate programming a heating cycle at 10°C/min within 25°C and 225°C. Thermoactuation performances of the samples were evaluated by acquiring an image every 10°C with a digital camera Pentax K500. The sample displacement was analyzed using ImageJ software.

4.6 | Photo actuation

The developed tension σ (Equation (2)) under irradiation by the LCEs were recorded in a custom-made setup previously described,[32,47,49] consisting in a force transducer (WPI KG4, 0–50 mN scale) where a LCE strip was attached and held in isometric condition by 2 clamps. Two M470L5 lamps Thorlabs were used to irradiate the materials simultaneously on both sides. The activation was controlled by a LabVIEW

program with a multichannel driver. Data reported are obtained by irradiation of the material with pulsed light from 2.3 mW/mm^2 to 15.9 mW/mm^2.

$$\sigma = F/A_{cs} \quad (2)$$

where F stands for absolute Force registered (mN), A_{cs} is the irradiated sample area (mm^2), or cross section.

4.7 | Thermal camera

The surface temperature of the samples during irradiation were recorded using a FLIR A500 streaming thermal imaging camera. The test was carried out under the same conditions as the photoactuation setup, using three optical power densities during a stimulation of 8 s.

For the beam steering set up a white polystyrene square (dimension 3 × 3 × 1 mm) was glued with Marabu Fixogum Rubber Cement at the tip of LCE strips (dimension 13 × 2 × 0.05 mm) and the specimens were coated with gold layer of 50 μm using sputter coater (Quorum Sputter QT150, Quorum Technologies Ltd, UK). The sample was attached to a drilled holder with a black tape. A red light source at 633 nm (HRP050, Thorlabs) is focused on the gold mirror at the lower end of the specimen and deflected at a 45° angle of reflection onto a millimeter panel. On the opposite surface, the sample was irradiated with a blue light source at 470 nm (MDLIII, CNI Optoelectric Technologies) to photoactuate the LCE and produce a change in the reflection angle of the incident red beam.

AUTHOR CONTRIBUTIONS

Giovanni Simonetti: Writing—original draft; investigation; data curation. **Ruggero Rossi**: Investigation; writing—original draft; data curation. **Daniele Martella**: Conceptualization; supervision; writing—review and editing; methodology. **Caterina Credi**: Conceptualization; writing—review and editing; supervision. **Cecilia Ferrantini**: Conceptualization; writing—review and editing; methodology. **Federico Carpi**: Conceptualization; writing—review and editing; methodology. **Camilla Parmeggiani**: Conceptualization; writing—review and editing; supervision; resources; funding acquisition; methodology.

ACKNOWLEDGMENTS

This work has received funding from the European Union under the Horizon 2020 research and innovation programme, grant agreement No. 95216 (REPAIR), and from the European Union—NextGenerationEU under the National Recovery and Resilience Plan (PNRR)—Mission 4 Education and research—Component 2 From research to business—Investment 1.1 Notice Prin 2022—DD N. 104 del 02/02/2022, from the project "ALICE—light-Activated high-performance actuators by electrospinning of reversibly crosslinked Liquid CrystallinE networks", proposal code 20224EBZ3Y—CUP J53D23008450006. The financial support provided by the MUR—Dipartimenti di Eccellenza 2023-2027 to the Department of Chemistry "Ugo Schiff" (DICUS 2.0) and to the Department of Experimental and Clinical Medicine of the University of Florence is acknowledged. Finanziamento di Ateneo Unifi Grandi Attrezzature 2021 was also acknowledged.

CONFLICT OF INTEREST STATEMENT

The authors declare no conflicts of interest.

DATA AVAILABILITY STATEMENT

The data that supports the findings of this study are available in the supplementary material of this article.

ORCID

Giovanni Simonetti https://orcid.org/0009-0005-0897-0719
Ruggero Rossi https://orcid.org/0009-0006-6674-3319
Daniele Martella https://orcid.org/0000-0002-8845-0908
Caterina Credi https://orcid.org/0000-0003-4565-5214
Cecilia Ferrantini https://orcid.org/0000-0002-3757-1363
Federico Carpi https://orcid.org/0000-0001-8496-5085
Camilla Parmeggiani https://orcid.org/0000-0002-1443-1878

REFERENCES

1. D. Liu, D. J. Broer, *Langmuir* **2014**, *30*, 13499.
2. J. Gao, Y. Tang, D. Martella, J. Guo, D. S. Wiersma, Q. Li, *Responsive Mater.* **2023**, *1*, e20230008.
3. R. Wang, Z. Lei, J. Jiang, C. Peng, *Responsive Mater.* **2025**, *3*, e20250001.
4. M. López-Valdeolivas, D. Liu, D. J. Broer, C. Sánchez-Somolinos, *Macromol. Rapid Commun.* **2018**, *39*.
5. Y. He, H. Liu, J. Luo, N. Li, Z. Zhang, J. Gan, Z. Yang, *Adv. Mater. Technol.* **2024**, *9*, 2400073.
6. D. J. Roach, C. Yuan, X. Kuang, V. C.-F. Li, P. Blake, M. L. Romero, I. Hammel, K. Yu, H. J. Qi, *ACS Appl. Mater. Interfaces* **2019**, *11*, 19514.
7. P. Lyu, M. O. Astam, C. Sánchez-Somolinos, D. Liu, *Adv. Intell. Syst.* **2022**, *4*, 2200280.
8. S. Nocentini, D. Martella, D. S. Wiersma, C. Parmeggiani, *Soft Matter* **2017**, *13*, 8590.
9. T. Guin, M. J. Settle, B. A. Kowalski, A. D. Auguste, R. V. Beblo, G. W. Reich, T. J. White, *Nat. Commun.* **2018**, *9*, 2531.
10. K. Urayama, R. Mashita, I. Kobayashi, T. Takigawa, *Macromolecules* **2007**, *40*, 7665.
11. J. A. Herman, R. Telles, C. C. Cook, S. C. Leguizamon, J. A. Lewis, B. Kaehr, T. J. White, D. J. Roach, *Adv. Mater.* **2024**, *36*, 2414209.
12. M. Del Pozo, J. A. H. P. Sol, A. P. H. J. Schenning, M. G. Debije, *Adv. Mater. Deerfield Beach Fla.* **2022**, *34*, e2104390.
13. L. McDougall, J. Herman, E. Huntley, S. Leguizamon, A. Cook, T. White, B. Kaehr, D. J. Roach, *ACS Appl. Mater. Interfaces* **2023**, *15*, 58897.
14. Y. Yang, S. Zhang, Y. Ji, Y. Wei, J. Wang, X. He, *Mater. Today* **2024**, *74*, 167.
15. C. Ohm, M. Brehmer, R. Zentel, *Adv. Mater.* **2010**, *22*, 3366.
16. L. Ceamanos, Z. Kahveci, M. López-Valdeolivas, D. Liu, D. J. Broer, C. Sánchez-Somolinos, *ACS Appl. Mater. Interfaces* **2020**, *12*, 44195.
17. L. Chen, J. Liu, M. Cheng, Z. Wang, W. Cai, Z. Ma, Z. Bai, D. Kong, M. Cen, Y. J. Liu, *Opt. Express* **2024**, *32*, 12528.
18. H. Zeng, P. Wasylczyk, C. Parmeggiani, D. Martella, M. Burresi, D. S. Wiersma, *Adv. Mater. Deerfield Beach Fla.* **2015**, *27*, 3883.

19. J. G. Kim, J. Jeon, R. Sivakumar, J. Lee, Y. H. Kim, M. Cho, J. H. Youk, J. J. Wie, *Adv. Intell. Syst.* **2022**, *4*, 2100148.
20. O. M. Wani, H. Zeng, A. Priimagi, *Nat. Commun.* **2017**, *8*, 15546.
21. J. Jeon, J.-C. Choi, H. Lee, W. Cho, K. Lee, J. G. Kim, J.-W. Lee, K.-I. Joo, M. Cho, H.-R. Kim, J. J. Wie, *Mater. Today* **2021**, *49*, 97.
22. C. P. Ambulo, J. J. Burroughs, J. M. Boothby, H. Kim, M. R. Shankar, T. H. Ware, *ACS Appl. Mater. Interfaces* **2017**, *9*, 37332.
23. G. E. Bauman, J. M. McCracken, T. J. White, *Angew. Chem. Int. Ed.* **2022**, *61*, e202202577.
24. X. Peng, X. Kuang, D. J. Roach, Y. Wang, C. M. Hamel, C. Lu, H. J. Qi, *Addit. Manuf.* **2021**, *40*, 101911.
25. I. Zubritskaya, D. Martella, S. Nocentini, *ACS Appl. Mater. Interfaces* **2025**, *17*, 11100.
26. C. L. van Oosten, C. W. M. Bastiaansen, D. J. Broer, *Nat. Mater.* **2009**, *8*, 677.
27. X. Lu, C. P. Ambulo, S. Wang, L. K. Rivera-Tarazona, H. Kim, K. Searles, T. H. Ware, *Angew. Chem. Int. Ed.* **2021**, *60*, 5536.
28. X. Wang, Y. Yao, Y. Zhang, W. Wang, S. Bi, G. Shao, J. Jiang, N. Chen, H. Shao, *Chem. Eng. J.* **2024**, *499*, 156180.
29. M. C. Escobar, T. J. White, *Adv. Mater.* **2024**, *36*, 2401140.
30. Y. Chen, J. Jiang, Y. Zhao, *Macromolecules* **2024**, *57*, 10539.
31. A. Velasco Abadia, G. E. Bauman, T. J. White, D. K. Schwartz, J. L. Kaar, *Adv. Mater. Interfaces* **2023**, *10*, 2300086.
32. S. Donato, D. Martella, M. Salzano de Luna, G. Arecchi, S. Querceto, C. Ferrantini, L. Sacconi, P.-L. Brient, C. Chatard, A. Graillot, D. S. Wiersma, C. Parmeggiani, *Macromol. Rapid Commun.* **2023**, *44*, 2200958.
33. N. P. Skillin, G. E. Bauman, B. E. Kirkpatrick, J. M. McCracken, K. Park, R. A. Vaia, K. S. Anseth, T. J. White, *Adv. Mater.* **2024**, *36*, 2313745.
34. A. Das, J. M. McCracken, M. H. Saeed, D. Nepal, T. J. White, *Angew. Chem.* **2025**, *137*, e202505300.
35. M. Pilz Da Cunha, E. A. J. Van Thoor, M. G. Debije, D. J. Broer, A. P. H. J. Schenning, *J. Mater. Chem. C* **2019**, *7*, 13502.
36. P. Sartori, R. Singh Yadav, J. del Barrio, A. DeSimone, C. Sánchez-Somolinos, **2024**.
37. L. Montesino, J. I. Martínez, C. Sánchez-Somolinos, *Adv. Funct. Mater.* **2024**, *34*, 2470051.
38. S. J. D. Lugger, L. Ceamanos, D. J. Mulder, C. Sánchez-Somolinos, A. P. H. J. Schenning, *Adv. Mater. Technol.* **2023**, *8*, 2201472.
39. Z. Hu, Y. Li, J. Lv, *Nat. Commun.* **2021**, *12*, 3211.
40. R. Lan, J. Sun, C. Shen, R. Huang, Z. Zhang, L. Zhang, L. Wang, H. Yang, *Adv. Mater.* **2020**, *32*, 1906319.
41. T. J. White, N. V. Tabiryan, S. V. Serak, U. A. Hrozhyk, V. P. Tondiglia, H. Koerner, R. A. Vaia, T. J. Bunning, *Soft Matter* **2008**, *4*, 1796.
42. G. Feregotto, G. Simonetti, R. Rossi, D. Martella, C. Credi, C. Parmeggiani, F. Carpi, in *3D Print. Bioprinting Med. Surg.* (Eds:M. Carfagni, S. Celi, M. Servi, M. Mencarelli), Springer Nature Switzerland, Cham **2025**, pp. 33–44.
43. S. Donato, R. Bini, G. Simonetti, N. Fuochi, M. Salzano de Luna, C. Chatard, P.-L. Brient, D. S. Wiersma, D. Martella, C. Parmeggiani, *Macromolecules* **2025**, *58*, 9672.
44. G. Wang, M. L. McCain, L. Yang, A. He, F. S. Pasqualini, A. Agarwal, H. Yuan, D. Jiang, D. Zhang, L. Zangi, J. Geva, A. E. Roberts, Q. Ma, J. Ding, J. Chen, D.-Z. Wang, K. Li, J. Wang, R. J. A. Wanders, W. Kulik, F. M. Vaz, M. A. Laflamme, C. E. Murry, K. R. Chien, R. I. Kelley, G. M. Church, K. K. Parker, W. T. Pu, *Nat. Med.* **2014**, *20*, 616.
45. Z. Zhang, Y. Wang, Q. Wang, L. Shang, *Small* **2022**, *18*, 2105116.
46. C. Ferrantini, J. M. Pioner, D. Martella, R. Coppini, N. Piroddi, P. Paoli, M. Calamai, F. S. Pavone, D. S. Wiersma, C. Tesi, E. Cerbai, C. Poggesi, L. Sacconi, C. Parmeggiani, *Circ. Res.* **2019**, *124*, e44.
47. M. Turriani, N. Cosottini, N. Fuochi, D. S. Wiersma, D. Martella, C. Parmeggiani, *Soft Matter* **2025**, *21*, 1162.
48. K. M. Lee, T. J. White, *Macromolecules* **2012**, *45*, 7163.
49. G. Vitale, B. Grandinetti, S. Querceto, D. Martella, C. Tesi, C. Poggesi, E. Cerbai, D. S. Wiersma, C. Parmeggiani, C. Ferrantini, L. Sacconi, *Macromol. Mater. Eng.* **2022**, *307*, 2200187.

SUPPORTING INFORMATION

Additional supporting information can be found online in the Supporting Information section at the end of this article.

How to cite this article: G. Simonetti, R. Rossi, D. Martella, C. Credi, C. Ferrantini, F. Carpi, C. Parmeggiani, *Responsive Mater*. **2026**, e70039. https://doi.org/10.1002/rpm2.70039